INTERNATIONAL JOURNAL FOR NUMERICAL METHODS IN FLUIDS
Int. J. Numer. Meth. Fluids 2009; **59**:1299–1320
Published online 5 August 2008 in Wiley InterScience (www.interscience.wiley.com). DOI: 10.1002/fld.1867

A viscous vortex particle method for deforming bodies with application to biolocomotion

Li Jeany Zhang*,† and Jeff D. Eldredge

Mechanical & Aerospace Engineering Department, University of California, Los Angeles, CA 90095, U.S.A.

SUMMARY

Bio-inspired mechanics of locomotion generally consist of the interaction of flexible structures with the surrounding fluid to generate propulsive forces. In this work, we extend, for the first time, the viscous vortex particle method (VVPM) to continuously deforming two-dimensional bodies. The VVPM is a high-fidelity Navier–Stokes computational method that captures the fluid motion through evolution of vorticity-bearing computational particles. The kinematics of the deforming body surface are accounted for via a surface integral in the Biot–Savart velocity. The spurious slip velocity in each time step is removed by computing an equivalent vortex sheet and allowing it to flux to adjacent particles; hence, no-slip boundary conditions are enforced. Particles of both uniform and variable size are utilized, and their relative merits are considered. The placement of this method in the larger class of immersed boundary methods is explored. Validation of the method is carried out on the problem of a periodically deforming circular cylinder immersed in a stagnant fluid, for which an analytical solution exists when the deformations are small. We show that the computed vorticity and velocity of this motion are both in excellent agreement with the analytical solution. Finally, we explore the fluid dynamics of a simple fish-like shape undergoing undulatory motion when immersed in a uniform free stream, to demonstrate the application of the method to investigations of biomorphic locomotion. Copyright © 2008 John Wiley & Sons, Ltd.

Received 27 November 2007; Revised 19 March 2008; Accepted 25 May 2008

KEY WORDS: vortex particle methods; biological locomotion; immersed boundary methods; numerical methods; viscous incompressible flow; flow–structure interaction

1. INTRODUCTION

Biological locomotion mechanics at moderate Reynolds number, as evident in creatures such as insects and fish, is fundamentally based on the reaction force supplied by the fluid against an accelerating and deforming surface. For example, the undulatory wave sent from the head to the tail of an eel causes an oscillatory exchange of energy with the adjacent fluid, resulting in a net

*Correspondence to: Li Jeany Zhang, Mechanical & Aerospace Engineering Department, University of California, Los Angeles, CA 90095, U.S.A.
†E-mail: lijeany@ucla.edu

forward thrust from the unbalanced tail motion [1]. This tail motion shares many common features with the wing kinematics of a hovering insect, characterized by flapping in a horizontal stroke plane to produce a net lift [2]. Vorticity production and shedding are a hallmark of the flows produced by these mechanisms [3]. Previous investigations have revealed that the manner in which vorticity is produced and processed by the flapping or undulating surface has a profound effect on the thrust efficiency of a swimming organism [4] and lift generation of a flapping insect wing [5]. The flexibility of the creature's body and appendages almost certainly modulates this vorticity interaction, though to what extent is still unclear. It is also unclear under what circumstances the creature is actively controlling its body shape or allows it to respond passively to the adjacent flow. This mix of active and passive flexibilities has important implications in the energy efficiency of locomotion.

The computational tool presented in this work, an extension of the viscous vortex particle method (VVPM) to two-dimensional deforming bodies, is motivated by the desire to address such questions. Computational approaches that focus on vorticity have a natural appeal for moderate-Reynolds number biolocomotion studies, in light of the demonstrated relevance of this quantity. Vortex particle methods [6–9] represent the evolution of a fluid flow by the advection of regularized vorticity-bearing particles. The particle formulation enables a natural adaptability to the flow. A number of critical developments in the past 20 years have enabled vortex particle methods for high-fidelity Navier–Stokes simulations. The computation of the particle velocities through the Biot–Savart integral, which is inherently an $O(N^2)$ process, is accelerated to $O(N)$ with the help of the fast multipole method [10, 11]. Viscous diffusion (and other transport processes) can be modeled to arbitrary order of accuracy by the technique of particle strength exchange [12, 13]. For enforcement of boundary conditions at an impenetrable no-slip surface, Koutmoutsakos *et al*. [14] developed a technique of identifying the spurious slip velocity with an equivalent vortex sheet and then allowing the sheet vorticity to flux to the adjacent vortex particles.

The vorticity creation technique developed in [14] works, in principle, regardless of whether the body is rigid or deforming. In spite of this, many previous applications of the method (e.g. [15–17]) have focused exclusively on the flow past rigid bodies of relatively simple shape, in part because these implementations relied on distributions of particles that initially conformed to the body shape. Associated with such distributions are remeshing kernels with special constructions near boundaries. However, recent studies [18, 19] have shown that such special constructions are largely unnecessary, as the vorticity creation process has an inherent 'self-corrective' feature in each time step. Particles are instead allowed to start at the nodes of a Cartesian grid. Any circulation leaked into the body by particles that overlap the surface is immediately redistributed to the adjacent particles during the subsequent flux of the surface vortex sheet [16, 17, 19]. The price for this simplicity is that the method reverts to first-order accuracy in the vicinity of the body.

It is hoped that the VVPM methodology, as extended in this work and in future work, will provide a complementary numerical tool to methods developed for fluid–structure interaction in previous studies. For example, the arbitrary Lagrangian–Eulerian methods (ALE) and immersed boundary (IB) methods are two classes of methods to address solid surface deformations adjacent to the fluid. ALE methods reconstruct a mesh to allow local adaptation to the motion of solid structures. These methods allow high-order accuracy but only allow relatively small deformations, and remeshing is still required to eliminate badly distorted elements. The IB methods, in contrast, permit larger deformations, in that they treat solid boundaries as distributed force functions in a single computational domain that covers both the body and fluid. However, accuracy greater than first order is difficult to achieve. Furthermore, because of the isotropic grid setup near the

DOI: 10.1002/fld

body surface, IB methods cannot be easily applied to high Reynolds number flows, for which boundary layers are thin. Both methods have been broadly utilized and successfully applied to numerous problems in biological locomotion [20–24]. The method proposed in this work is not meant to replace these existing methods, but to complement them. Cottet [25] has shown that the vortex particle method can be a powerful tool to explore fluid–structure interactions because of their allowance for large deformations. He incorporated an IB approach into the vortex particle method and compared it with ALE methods in a simple one-dimensional Burger's equation coupled with linear elasticity. In our work, the influence of body motion is partially accounted for via a surface integral in the velocity expression, but the presence of the body is communicated by vorticity creation and flux to adjacent particles. This approach can be shown equivalent to an IB method [26].

The initial distribution of particles in the VVPM need not conform to the surface, and their subsequent convection allows a natural adaptivity, which makes them well suited for flows around complex (and, in particular, deforming) shapes. This paper presents a VVPM for two-dimensional deforming bodies. The principal new development is a recasting of the surface influence in the Biot–Savart integral, with an associated change in the equation for the vortex sheet strength. The method is validated on the problem of a circular cylinder undergoing small periodic shape deformation in a quiescent fluid; the analytical solution of this problem is presented in Appendix A. The error of the method is explored using both a Cartesian and a polar mapping of the particles. The method is finally demonstrated on the undulatory shape change of a fish-like body immersed in a uniform free stream.

2. METHODOLOGY

In this section, the VVPM for two-dimensional deforming bodies is presented. The presentation focuses on new developments, particularly the use of a surface-modified version of the Biot–Savart integral for computing the velocity field. Details of the other aspects of the method are omitted, and the reader is referred to previous work, notably [8].

2.1. General governing equations

VVPMs solve the Lagrangian form of the Navier–Stokes equations and utilize vorticity-carrying particles as computational elements. In particle form, the equations are written as separate convection and diffusion problems that evolve the particle positions $\mathbf{x}_p$ and vorticities $\boldsymbol{\omega}_p$. These equations are usually solved by a viscous splitting algorithm in substeps: particles are convected by the velocity field $\mathbf{u}$ over a small time step, and then particle strength exchange [12] is used to approximate the Laplacian operator in the diffusion problem on the static particles. The no-slip boundary conditions are enforced by solving for and fluxing a vortex sheet into adjacent particles in the fluid.

For a flow past a general body in motion, the velocity $\mathbf{u}$ includes particle-induced velocity $\mathbf{u}_\omega$, velocity due to a vortex sheet on the body surface, $\mathbf{u}_\gamma$, velocity induced by the deformation of the surface, $\mathbf{u}_s$, and free stream velocity $\mathbf{U}_\infty$,

$$\mathbf{u} = \mathbf{u}_\omega + \mathbf{u}_\gamma + \mathbf{u}_s + \mathbf{U}_\infty \tag{1}$$

The contribution from the particles, $\mathbf{u}_\omega$, is expressed in terms of a discrete version of the Biot–Savart integral. The surface vortex sheet contribution, $\mathbf{u}_\gamma$, is a surface integral with a

DOI: 10.1002/fld

Biot–Savart kernel. When the body is rigid, the only contribution to $\mathbf{u}_s$ is due to the rotation of the body; in such circumstances, the region occupied by the body interior can be regarded as a patch of uniform vorticity, equal to twice the angular velocity, and $\mathbf{u}_s$ is then expressed via a Biot–Savart integral over the body interior.

When the body is deforming, however, $\mathbf{u}_s$ cannot be simply expressed in terms of interior vorticity. It is more natural to express it as an integral over the body surface, relying only on the kinematics of the deforming surface. Suppose that S_b denotes a closed surface and V_f represents an external fluid region. We seek an expression for velocity $\mathbf{u}_s(\mathbf{x})$ when $\mathbf{x}\in V_f$. In order to derive the contribution from the body deformation, the only assumptions we make is that $\nabla\cdot\mathbf{u}=0$ in V_f and that the deformation is volume-preserving.

Using Cartesian index notation, we can write

$$\frac{\partial}{\partial x_j}\left[u_i(\mathbf{x})\frac{\partial}{\partial x_j}G(\mathbf{x},\mathbf{x}')-G(\mathbf{x},\mathbf{x}')\frac{\partial u_i}{\partial x_j}(\mathbf{x}')\right]=-u_i(\mathbf{x})\delta(\mathbf{x}-\mathbf{x}')+G(\mathbf{x},\mathbf{x}')(\nabla\times\boldsymbol{\omega})_i \tag{2}$$

where $G(\mathbf{x},\mathbf{x}')$ is Green's function for the negative Laplacian, that is, $\nabla^2 G=-\delta$. By integrating the above equation over V_f, applying the divergence theorem and switching $\mathbf{x}$ and $\mathbf{x}'$, we arrive at

$$\begin{aligned}\mathbf{u}(\mathbf{x})=\nabla\times\int_{V_f}G(\mathbf{x},\mathbf{x}')\boldsymbol{\omega}(\mathbf{x}')\,\mathrm{d}V(\mathbf{x}')\\ +\int_{S_b}[-(\mathbf{n}'\times\boldsymbol{\omega}(\mathbf{x}'))G(\mathbf{x},\mathbf{x}')+\mathbf{u}(\mathbf{x}')(\mathbf{n}'\cdot\nabla' G(\mathbf{x},\mathbf{x}'))-(\mathbf{n}'\cdot\nabla'\mathbf{u})G(\mathbf{x},\mathbf{x}')]\,\mathrm{d}S(\mathbf{x}')\end{aligned} \tag{3}$$

where $\mathbf{n}'$ denotes the normal vector at $\mathbf{x}'\in S_b$ directed into V_f. It should be noted that $\mathbf{n}'\cdot\nabla'\mathbf{u}$ represents the normal derivative of the velocity (evaluated from the fluid side) at the surface point $\mathbf{x}'$.

We seek a simpler form for the surface integral in Equation (3), which we denote by $\mathbf{u}_B(\mathbf{x})$. It is noted that $\mathbf{n}\times(\nabla\times\mathbf{u})+\mathbf{n}\cdot\nabla\mathbf{u}=\mathbf{n}\cdot(\nabla\mathbf{u})^{\mathrm{T}}$, hence, the integral becomes

$$\mathbf{u}_B(\mathbf{x})=\int_{S_b}[-\mathbf{n}'\cdot(\nabla'\mathbf{u})^{\mathrm{T}}G(\mathbf{x},\mathbf{x}')+\mathbf{u}(\mathbf{x}')(\mathbf{n}'\cdot\nabla' G)]\,\mathrm{d}S(\mathbf{x}') \tag{4}$$

The first term of the above surface integral can be further manipulated. Its ith component can be written, using the divergence theorem to convert to a volume integral and back again to a surface integral, as

$$\begin{aligned}\int_{V_f}\frac{\partial}{\partial x'_j}\left(\frac{\partial u_j}{\partial x'_i}G\right)\mathrm{d}V(\mathbf{x}')&=\int_{V_f}\left[\frac{\partial^2}{\partial x'_i\partial x'_j}(u_j G)-\frac{\partial}{\partial x'_j}\left(u_j\frac{\partial G}{\partial x'_i}\right)\right]\mathrm{d}V(\mathbf{x}')\\ &=\int_{V_f}\left[\frac{\partial}{\partial x'_i}\left(\frac{\partial u_j}{\partial x'_j}G+u_j\frac{\partial G}{\partial x'_j}\right)-\frac{\partial}{\partial x'_j}\left(u_j\frac{\partial G}{\partial x'_i}\right)\right]\mathrm{d}V(\mathbf{x}')\\ &=-\int_{S_b}\left(n'_i u_j\frac{\partial G}{\partial x'_j}+n'_j u_j\frac{\partial G}{\partial x'_i}\right)\mathrm{d}S(\mathbf{x}')\end{aligned} \tag{5}$$

DOI: 10.1002/fld

The divergence-free condition on velocity has been used in the final step. Thus, the complete surface integral $\mathbf{u}_B$ becomes

$$\int_{S_b}\left[n'_j u_j \frac{\partial G}{\partial x'_i}+\frac{\partial G}{\partial x'_j}(u_i n'_j-u_j n'_i)\right]\mathrm{d}S(\mathbf{x}') \tag{6}$$

Consequently, the revised contribution of body surface motion to a point in the fluid is given by

$$\mathbf{u}_B(\mathbf{x})=\int_{S_b}[\nabla G(\mathbf{x},\mathbf{x}')\times(\mathbf{n}'\times\mathbf{u}(\mathbf{x}'))-\nabla G(\mathbf{x},\mathbf{x}')(\mathbf{n}'\cdot\mathbf{u}(\mathbf{x}'))]\,\mathrm{d}S(\mathbf{x}') \tag{7}$$

This shows that $\mathbf{u}_B$ can be regarded as the contribution from surface distributions of vortex and source singularities.

The velocity in the integrand of (7) is that which is found when the surface is approached from within the fluid, which we denote by $\mathbf{u}^+$; the velocity obtained by approaching from within the body is $\mathbf{u}^-$, which is set equal to the local velocity of the deforming surface, $\mathbf{u}_b$. The kinematical condition of no-flow-through implies a jump in the tangential components of the velocities on either side of the surface, which is equal to the strength, $\boldsymbol{\gamma}$, of a vortex sheet, namely,

$$\mathbf{n}\cdot\mathbf{u}^+=\mathbf{n}\cdot\mathbf{u}_b \tag{8}$$

$$\mathbf{n}\times\mathbf{u}^+=\mathbf{n}\times\mathbf{u}_b+\boldsymbol{\gamma} \tag{9}$$

Thus, the velocity in the fluid can be rewritten as

$$\mathbf{u}(\mathbf{x})=\int_{V_f}\nabla G(\mathbf{x},\mathbf{x}')\times\boldsymbol{\omega}(\mathbf{x}')\,\mathrm{d}V(\mathbf{x}')+\int_{S_b}\nabla G(\mathbf{x},\mathbf{x}')\times\boldsymbol{\gamma}(\mathbf{x}')\,\mathrm{d}S(\mathbf{x}')+\mathbf{u}_s(\mathbf{x})+\mathbf{U}_\infty \tag{10}$$

which now splits the surface integral into a contribution from the surface vortex sheet and a contribution from the surface kinematics,

$$\mathbf{u}_s(\mathbf{x})=\int_{S_b}[\nabla G(\mathbf{x},\mathbf{x}')\times(\mathbf{n}'\times\mathbf{u}_b(\mathbf{x}'))-\nabla G(\mathbf{x},\mathbf{x}')(\mathbf{n}'\cdot\mathbf{u}_b(\mathbf{x}'))]\,\mathrm{d}S(\mathbf{x}') \tag{11}$$

It is important to stress that Equation (10), in contrast to previous implementations of vortex methods [14, 16, 19], contains no volume integrals over the interior of the body. Also, it is worth noting that, although this formulation has been derived by assuming volume-preserving deformations, it is possible to include the effect of volume-changing kinematics in the method.

2.2. *Identification of a surface vortex sheet*

When Equation (10) is evaluated at a point on the surface approached from within the body, x_s^-, the left-hand side vanishes, it takes the form

$$\begin{aligned}0=&\int_{V_f}\nabla G(\mathbf{x}_s,\mathbf{x}')\times\boldsymbol{\omega}(\mathbf{x}')\,\mathrm{d}V(\mathbf{x}')+\frac{1}{2}(\mathbf{n}\times\boldsymbol{\gamma})|_{\mathbf{x}_s}+\int_{S_b}\nabla G(\mathbf{x}_s,\mathbf{x}')\times\boldsymbol{\gamma}(\mathbf{x}')\,\mathrm{d}S(\mathbf{x}')\\&+\frac{1}{2}[\mathbf{n}\times(\mathbf{n}\times\mathbf{u}_b)-\mathbf{n}(\mathbf{n}\cdot\mathbf{u}_b)]|_{\mathbf{x}_s}+\mathbf{u}_s(\mathbf{x}_s)+\mathbf{U}_\infty\end{aligned} \tag{12}$$

DOI: 10.1002/fld

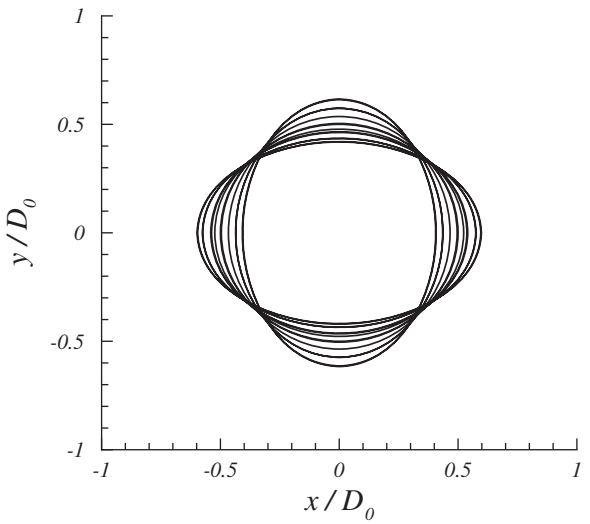

Figure 1. Oscillatory deformation of a circular cylinder, set at $a_0/R_0 = 0.2$ for demonstration purposes. Note that the actual deformation imposed in the simulation is $a_0/R_0 = 0.02$.

where the surface integrals are understood to be principal-value integrals. The expression in square brackets, which arose from evaluating $\mathbf{u}_s$ at $\mathbf{x}_s^-$, reduces simply to $-\mathbf{u}_b(\mathbf{x}_s)$. Consequently, the vector product of this equation with the local normal vector furnishes an integral equation for the surface vortex sheet strength:

$$\frac{1}{2}\boldsymbol{\gamma}(\mathbf{x}_s) - \mathbf{n} \times \int_{S_b} \nabla G(\mathbf{x}_s, \mathbf{x}') \times \boldsymbol{\gamma}(\mathbf{x}')\, \mathrm{d}S(\mathbf{x}')$$

$$= \left(\frac{1}{2}\mathbf{u}_b(\mathbf{x}_s) - \mathbf{u}_s(\mathbf{x}_s) - \int_{V_f} \nabla G(\mathbf{x}_s, \mathbf{x}') \times \boldsymbol{\omega}(\mathbf{x}')\, \mathrm{d}V(\mathbf{x}') \right) \times \mathbf{n} \tag{13}$$

where $\mathbf{u}_s$ is given by Equation (11). In practice, the surface integrals in this equation are discretized with flat boundary elements, and the vortex sheet strength is taken as uniform on each element. The volume integral is the classical Biot–Savart integral, and the particle representation of the vorticity leads to a discrete version of this integral. Although expressions (10) and (13) differ from those used for flow past a rigid body, the discretization procedures are the same. Details can be found in [19].

Equation (13) represents the identification of spurious slip with an equivalent vortex sheet with strength distribution $\boldsymbol{\gamma}$. Its formulation here differs from previous implementations, in that it entirely avoids volume integrals over the interior of the body. As in previous implementations [14, 16, 19], the slip is eliminated by fluxing the vorticity in this sheet to the adjacent fluid by solving a linear diffusion problem with Neumann boundary condition. Since the vortex sheet is the means by which this new circulation is introduced to the fluid, then we enforce Kelvin's circulation theorem during this process and account for circulation leaked into the body during the particle remeshing process by redistributing it to the particles when the vortex sheet is fluxed. The flux procedure utilizes a

DOI: 10.1002/fld

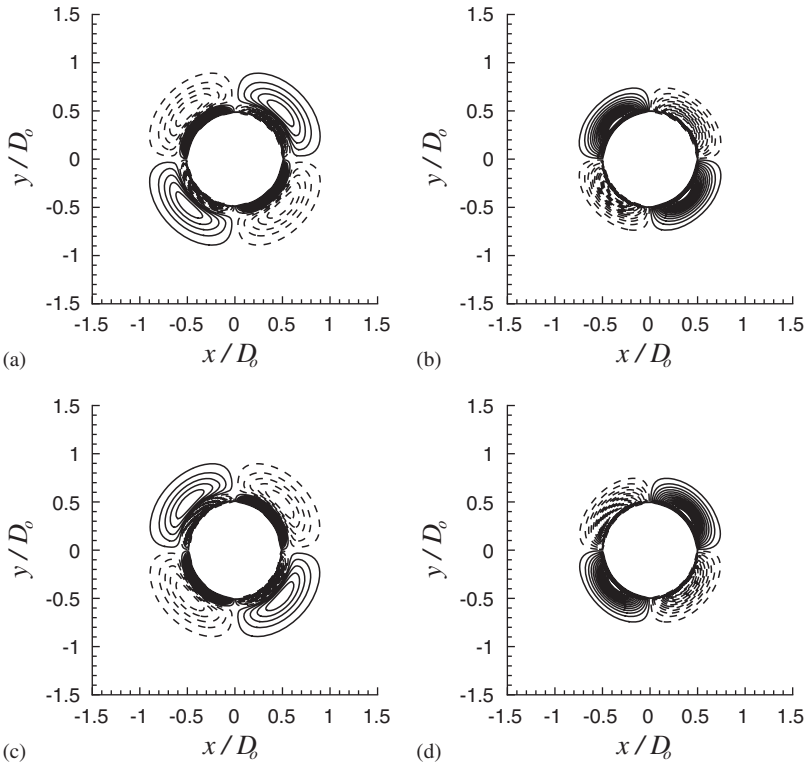

Figure 2. Vorticity contours at four instants for $Re_\Omega = 100$: (a) $t/T = 8.25$; (b) $t/T = 8.5$; (c) $t/T = 8.75$; and (d) $t/T = 9$.

semi-analytical scheme developed by Leonard *et al.* [27]. A correction is added to each particle in the vicinity of the panel to ensure strict conservation of the distributed panel strength [16].

3. RESULTS

This section presents the results of application of the VVPM for deforming bodies to two problems. The first problem consists of the oscillatory deformation of a circular cylinder immersed in a stagnant fluid. This problem admits an analytical solution for small deformation; hence, it is used as a validation for the numerical methodology. The second problem consists of a fish-like shape undergoing prescribed undulatory deformation in a uniform free stream.

3.1. Oscillatory deformation of a circular cylinder

Consider a closed curve described parametrically by

$$x_s(\phi, t) = a(t)\cos\phi \tag{14}$$

$$y_s(\phi, t) = b(t)\sin\phi \tag{15}$$

DOI: 10.1002/fld

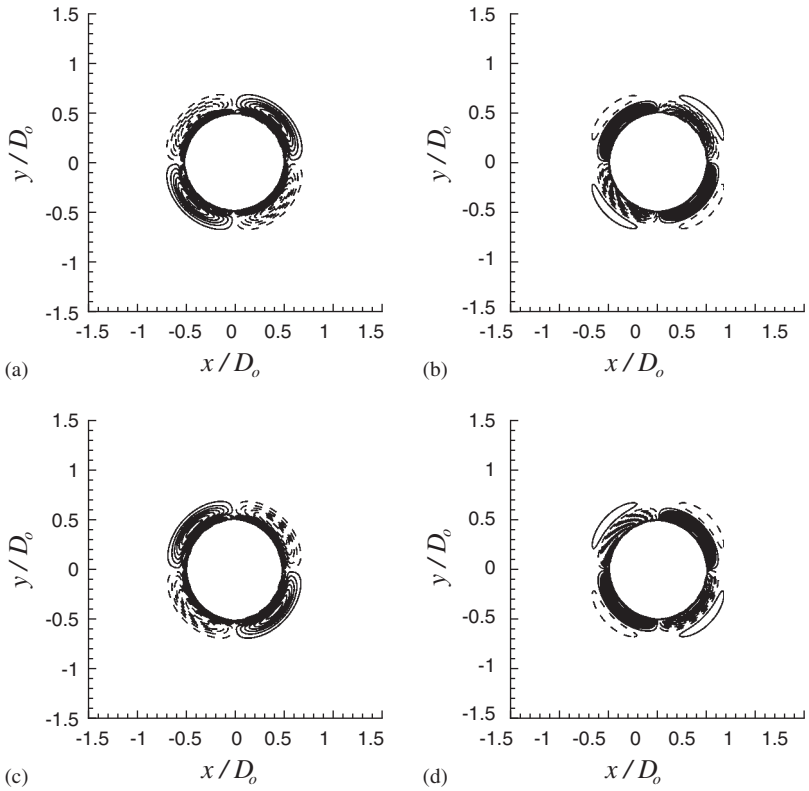

Figure 3. Vorticity contours at four instants for $Re_\Omega = 500$: (a) $t/T = 8.25$; (b) $t/T = 8.5$; (c) $t/T = 8.75$; and (d) $t/T = 9$.

where $\phi \in [-\pi, \pi)$. These equations describe the perimeter of an ellipse with time-varying semi-major and semi-minor axes $a(t)$ and $b(t)$, respectively. We prescribe $a(t)$ with a sinusoidal variation in time and constrain $b(t)$ to preserve the area enclosed by the curve

$$a(t) = R_0 + a_0 \sin(\Omega t) \tag{16}$$

$$b(t) = R_0^2 / a(t) \tag{17}$$

where R_0 is the radius of the initially circular shape of the curve. The prescribed surface velocity, $\mathbf{u}_b$, in Cartesian coordinates is $(\dot{a}\cos\phi, \dot{b}\sin\phi)$, where $\dot{()}$ denotes the time derivative. The Reynolds number in this problem is defined as $Re_\Omega = 4\Omega R_0^2/\nu$.

The problem is nondimensionalized by the oscillation frequency, Ω, and the initial radius, R_0 (vorticity contours by initial diameter D_0). When the deformation amplitude, a_0/R_0, is small, the polar angle θ is approximately equal to the parameter ϕ, and the surface velocity components

DOI: 10.1002/fld

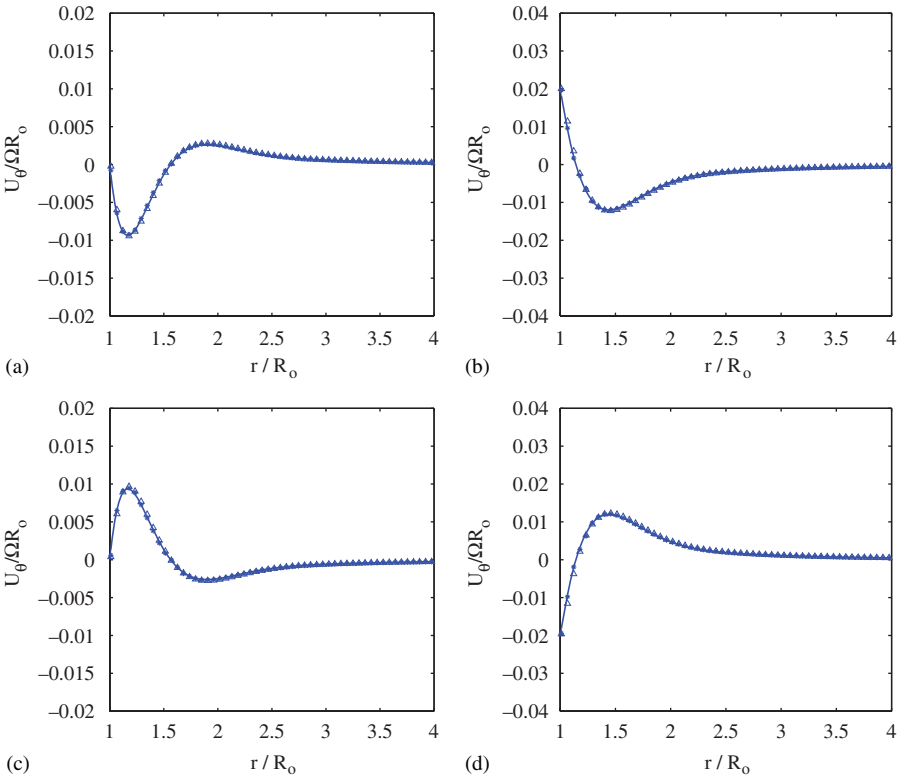

Figure 4. Circumferential velocity profile along $\theta=45°$ from $t/T=8.25$ to $t/T=9$ at $Re_\Omega=100$. Analytical solution, —; variable VVPM, ⋆; and uniform VVPM, △: (a) $t/T=8.25$; (b) $t/T=8.5$; (c) $t/T=8.75$; and (d) $t/T=9$.

(now in polar coordinates) have the approximate form

$$\frac{u_{s,r}(\theta,t)}{\Omega R_0}=\frac{a_0}{R_0}\cos\Omega t\cos 2\theta \tag{18}$$

$$\frac{u_{s,\theta}(\theta,t)}{\Omega R_0}=\frac{a_0}{R_0}\cos\Omega t\sin 2\theta \tag{19}$$

For such small deformation, the fluid has an approximately linear response. It can be shown that the velocity components and the vorticity of the resulting flow are

$$\frac{u_r(r,\theta,t)}{\Omega R_0}=2\frac{a_0}{R_0}Re[A_r(\kappa r)\exp(\mathrm{i}\Omega t)]\cos 2\theta \tag{20}$$

$$\frac{u_\theta(r,\theta,t)}{\Omega R_0}=2\frac{a_0}{R_0}Re[\mathrm{i}A_\theta(\kappa r)\exp(\mathrm{i}\Omega t)]\sin 2\theta \tag{21}$$

$$\frac{\omega(r,\theta,t)}{\Omega}=2\frac{a_0}{R_0}Re[\mathrm{i}W_+(\kappa r)\exp(\mathrm{i}\Omega t)]\sin 2\theta \tag{22}$$

DOI: 10.1002/fld

where $\kappa=(\Omega/\nu)^{1/2}$ is the wavenumber associated with viscous diffusion during the oscillation cycle ($T=2\pi$), and the radial eigenfunctions are

$$A_r(r)=-2\frac{\exp(\mathrm{i}\pi/4)}{K_1^+(\kappa R_0)}\frac{K_2^+(r)}{r}-\frac{1}{2}\frac{K_3^+(\kappa R_0)}{K_1^+(\kappa R_0)}\left(\frac{R_0}{r}\right)^3 \tag{23}$$

$$A_\theta(r)=-\mathrm{i}\frac{\exp(\mathrm{i}\pi/4)}{K_1^+(\kappa R_0)}K_2^{+'}(r)+\frac{\mathrm{i}}{2}\frac{K_3^+(\kappa R_0)}{K_1^+(\kappa R_0)}\left(\frac{R_0}{r}\right)^3 \tag{24}$$

$$W_+(r)=\frac{\kappa R_0\exp(\mathrm{i}\pi/4)}{K_1^+(\kappa R_0)}K_2^+(r) \tag{25}$$

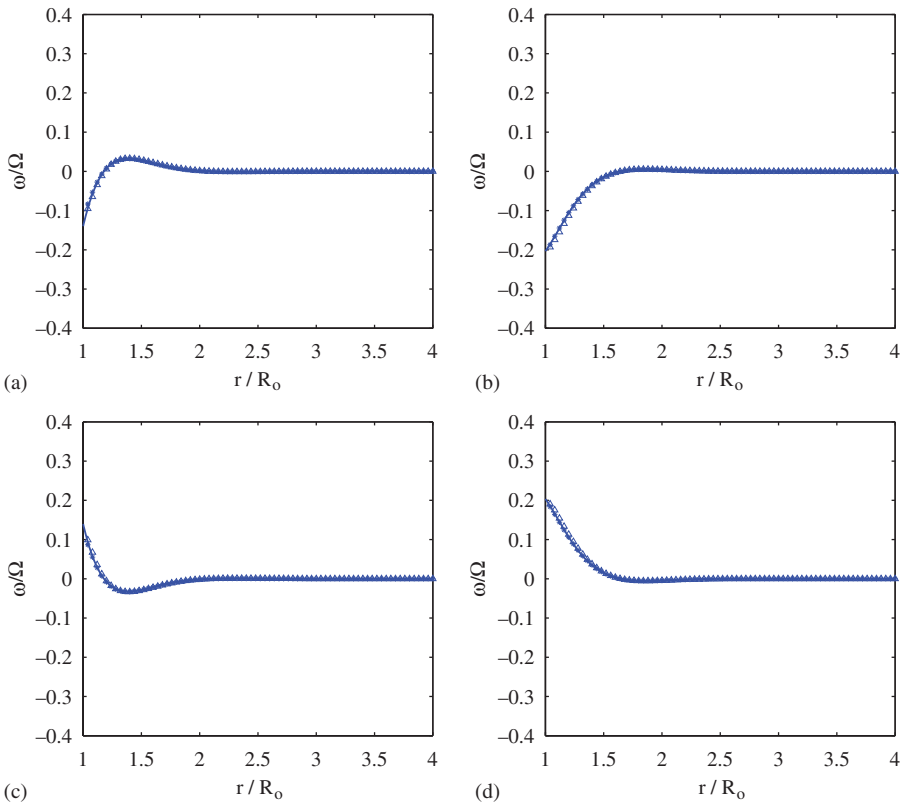

Figure 5. Vorticity profile along $\theta=45°$ from $t/T=8.25$ to $t/T=9$ at $Re_\Omega=100$. Analytical solution, —; variable VVPM, ⋆; and uniform VVPM, △: (a) $t/T=8.25$; (b) $t/T=8.5$; (c) $t/T=8.75$; and (d) $t/T=9$.

DOI: 10.1002/fld

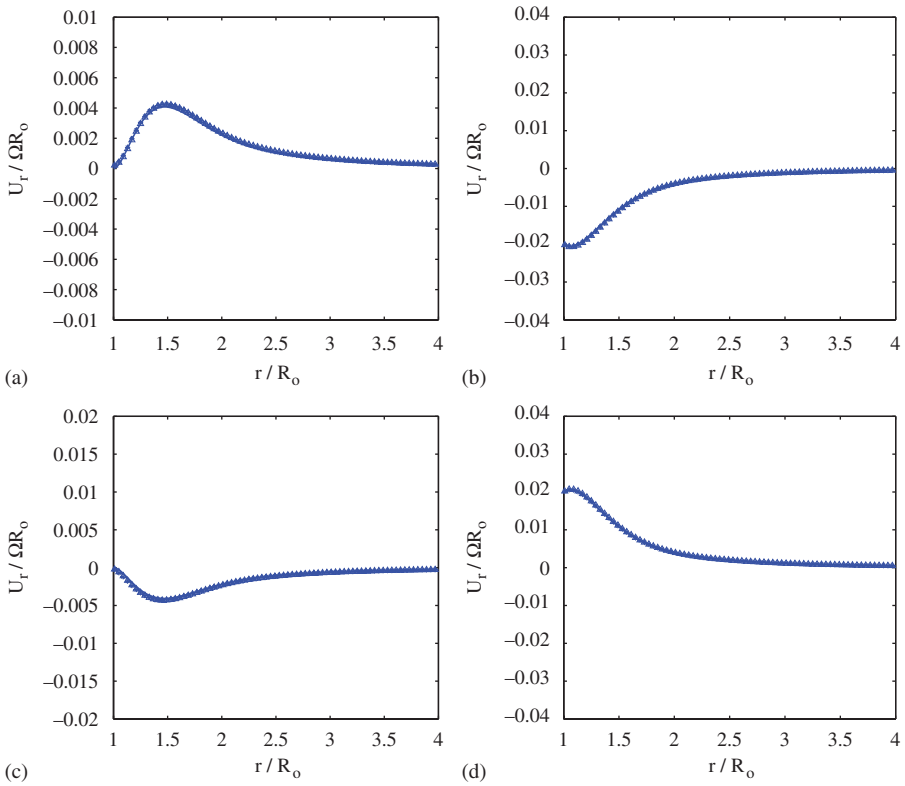

Figure 6. Radial velocity profile along $\theta = 0°$ from $t/T = 8.25$ to $t/T = 9$ at $Re_\Omega = 100$. Analytical solution, —; variable VVPM, ⋆; and uniform VVPM, △: (a) $t/T = 8.25$; (b) $t/T = 8.5$; (c) $t/T = 8.75$; and (d) $t/T = 9$.

Note that $\kappa R_0 = Re_\Omega^{1/2}/2$. The function K_n^+ is composed of Kelvin functions of the first kind

$$K_n^+(z) = \mathrm{ker}_n(z) + \mathrm{i}\,\mathrm{kei}_n(z) \tag{26}$$

In the present case, the deformation amplitude is set at $a_0/R_0 = 0.02$. Figure 1 illustrates a few instants of the deforming cylinder. To demonstrate the influence of particle distribution with respect to body shape, two different initial distributions were used. The first distribution consisted of particles of uniform size arranged on a uniform Cartesian grid. The second involved the use of a polar mapping suggested by Cottet *et al.* [28]

$$r = R_0 \exp \hat{x}, \quad \theta = \hat{y} \tag{27}$$

The particles are uniformly distributed in the domain $(0, \log(R_{\max}/R_0)) \times [-\pi, \pi)$ in the $(\hat{x}, \hat{y})$ computational space; the outer radius, $R_{\max}$, increases automatically as vorticity is diffused farther form the cylinder. This mapping ensures that adjacent particles maintain a nearly uniform separation from the deforming cylinder surface, thereby avoiding the loss of accuracy associated with particle overlap [19].

DOI: 10.1002/fld

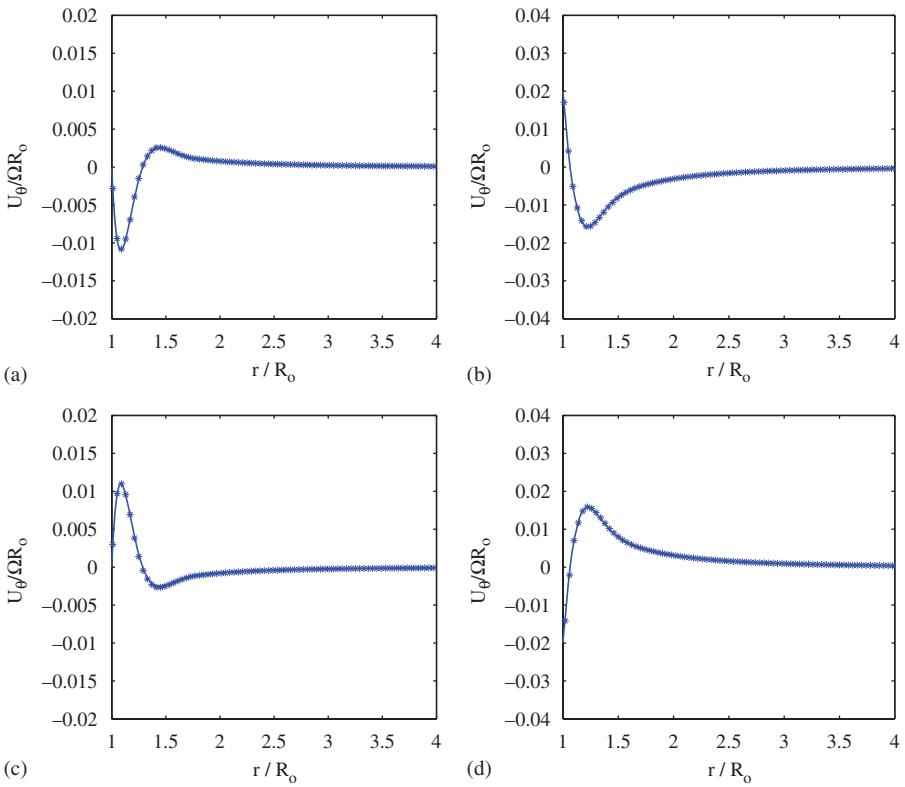

Figure 7. Circumferential velocity profile along $\theta = 45°$ from $t/T = 8.25$ to $t/T = 9$ at $Re_\Omega = 500$. Analytical solution, —; and variable VVPM, ⋆: (a) $t/T = 8.25$; (b) $t/T = 8.5$; (c) $t/T = 8.75$; and (d) $t/T = 9$.

Both particle distributions were utilized in the problem at $Re_\Omega = 100$. The particle spacing adjacent to the cylinder surface (and everywhere else in the case of the uniform distribution) was $\Delta x = 0.02R_0$, and the time step size was $\Delta t = 0.01/\Omega$. Contours of the vorticity field are depicted at four instants in the 9th oscillation cycle—after all initial transient behavior has decayed—in Figure 2. The problem was also simulated at $Re_\Omega = 500$, using only the variable-sized particle distribution. In this case, the thickness of the diffusion layer is comparatively smaller; hence, the particle spacing is adjusted according to $\Delta x = 0.008R_0$ and the time step size to $\Delta t = 0.016/\Omega$. The vorticity contours in Figure 3 clearly demonstrate the more compact layer.

The qualitative agreement between the VVPM results and the analytical solution is demonstrated by comparing flow profiles along polar lines. Figures 4–6 depict the velocity and vorticity profiles at $Re_\Omega = 100$ along the polar lines $\theta = 45$ or 0°, at four different instants within an oscillation period. All figures contain the comparison between the analytical solution and the results from both the variable- and uniform-sized particles in the VVPM. It is clear that the agreement is very good. The corresponding profiles at the higher Reynolds number of 500 are shown in Figures 7–9. Again, the results correspond closely.

The quantitative agreement of the VVPM results with the analytical solution was assessed by computing the L_2 error of u_r, labeled as ε_2. The results at both Reynolds numbers, $Re_\Omega = 100$ at

DOI: 10.1002/fld

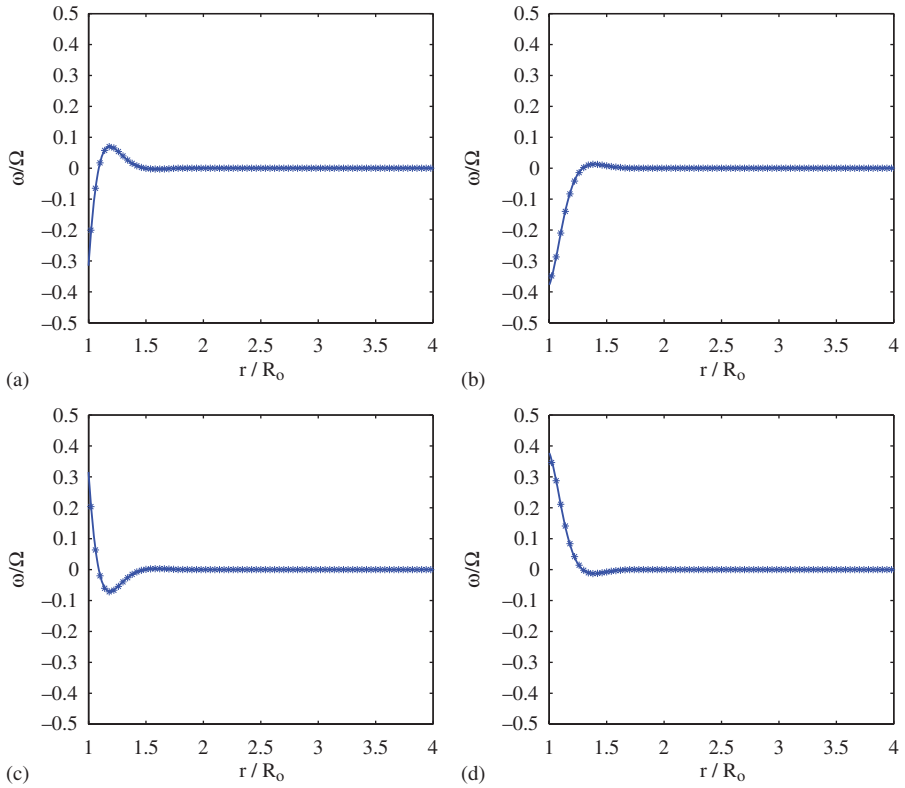

Figure 8. Vorticity profile along $\theta = 45°$ from $t/T = 8.25$ to $t/T = 9$ at $Re_\Omega = 500$. Analytical solution, —; and variable VVPM, ⋆: (a) $t/T = 8.25$; (b) $t/T = 8.5$; (c) $t/T = 8.75$; and (d) $t/T = 9$.

$t/T = 5.25$ and $Re_\Omega = 500$ at $t/T = 8.25$, are listed in Table I. The results for Reynolds number 100 versus Δx are plotted in Figure 10, where the variable-particle VVPM presents a power law of ε_2 with Δx at $\varepsilon_2 \sim \Delta x^{1.55}$ and the uniform-particle VVPM gives $\varepsilon_2 \sim \Delta x^{1.61}$.

In summary, the simulation results demonstrate good agreement with the analytical solution for a circular cylinder with small oscillatory deformation in a stagnant fluid at two different oscillation Reynolds numbers.

3.2. Undulating fish-like shape in uniform free stream

In order to demonstrate the utility of the VVPM with deforming bodies to problems of biolocomotion, we explore the flow produced by an undulating two-dimensional fish-like profile immersed in a uniform freestream. The profile of the fish is prescribed at all times. Its construction, depicted schematically in Figure 11, consists of first specifying the time-varying shape of a backbone curve, then generating a finite number of circles with constant radii at fixed locations along the backbone. The fish profile is generated by fitting cubic splines between fixed attachment points on the circles. Each circle has two attachment points at opposite ends of the diameter that is parallel to the

DOI: 10.1002/fld

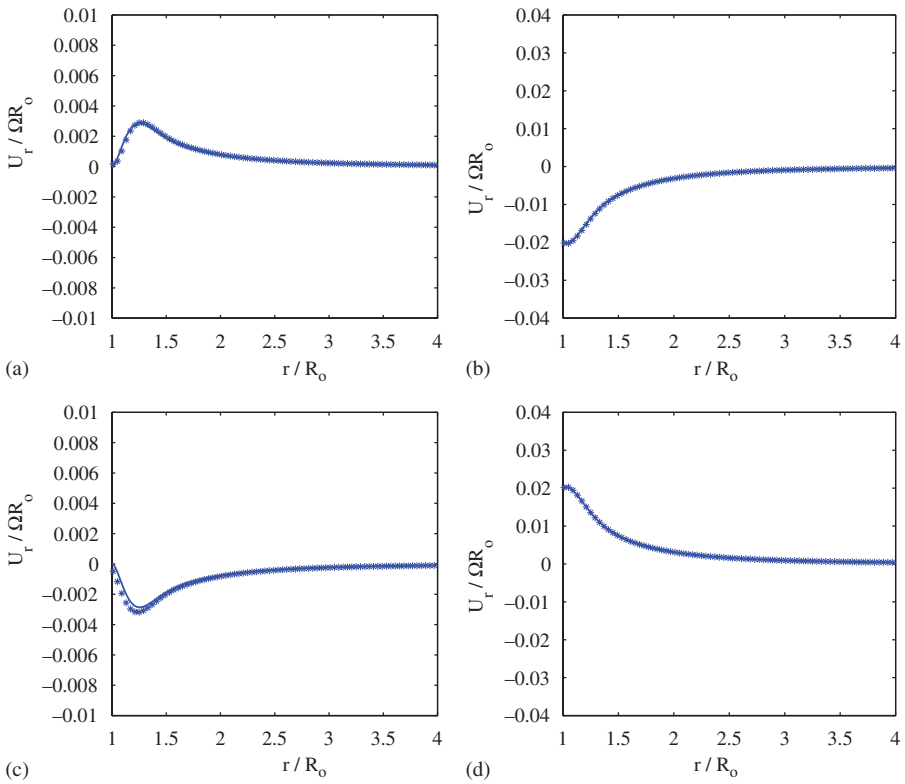

Figure 9. Radial velocity profile along $\theta = 0°$ from $t/T = 8.25$ to $t/T = 9$ at $Re_\Omega = 500$. Analytical solution, —; and variable VVPM, ⋆: (a) $t/T = 8.25$; (b) $t/T = 8.5$; (c) $t/T = 8.75$; and (d) $t/T = 9$.

backbone normal from the circle's origin; the first and last circles also have attachment points at the 'nose' and 'tail' of the fish. Each spline is divided into straight boundary elements for the purpose of surface integrals; the density of boundary elements is greater near the tail, where the radius of curvature is smallest. Note that this procedure does not guarantee that the area enclosed by the surface is preserved. However, it will be demonstrated below that the maximum area change is negligible for the shape changes considered in this study.

The backbone undulatory motion is given by

$$x_c(s,t) = -0.5 + s \tag{28}$$

$$y_c(s,t) = A_0 e^{ks} \sin[2\pi(s - ft)] \tag{29}$$

where the parameter s varies from 0 to 1, $A_0 = 0.05$ is the undulation amplitude, $k = 0.5$ is a growth factor, f is the frequency and the period is $T = 1/f$. This form, which is motivated by the analysis of carangiform fish mechanics by Lighthill [29], produces a traveling wave of growing amplitude that propagates from the head to the tail. By using this construction of a fish-like shape,

DOI: 10.1002/fld

Table I. L_2 Error of u_r along the polar line $\theta=0°$.

	Variable	Uniform
$Re_\Omega=100,\ \Delta x/R_0=0.01$	1.8388×10^{-5}	1.5990×10^{-5}
$Re_\Omega=100,\ \Delta x/R_0=0.02$	5.2311×10^{-5}	4.6607×10^{-5}
$Re_\Omega=100,\ \Delta x/R_0=0.03$	1.0274×10^{-4}	7.9676×10^{-5}
$Re_\Omega=100,\ \Delta x/R_0=0.04$	1.5552×10^{-4}	1.5975×10^{-4}
$Re_\Omega=500,\ \Delta x/R_0=0.008$	3.3603×10^{-5}	N/A

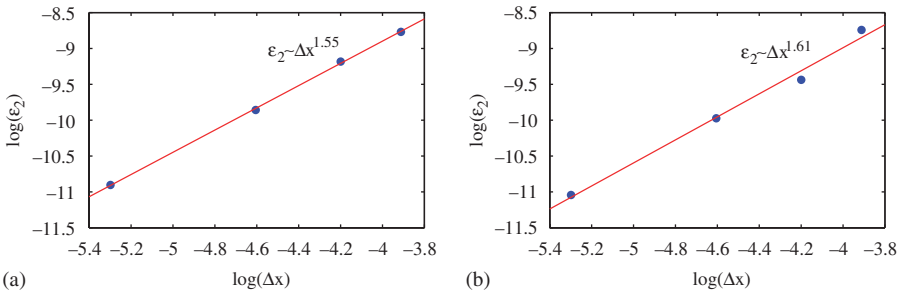

Figure 10. Convergence test by using L_2 error of u_r along polar line at 0° for VVPM at $Re_\Omega=100$: (a) VVPM with the variable-sized particles at $t/T=5.25$ and (b) VVPM with the uniform-sized particles at $t/T=5.25$.

the fractional change of area is bounded by $|A-\bar{A}|/\bar{A}<0.002$, and thus the body configuration can be regarded as area preserving.

In Appendix A, it is shown that the force exerted by the fluid on the fish surface is given by the following expression:

$$\mathbf{F}=-\rho_f\oint_{S_b}\left[(\mathbf{x}-\mathbf{X})\times\left(\frac{\gamma}{\Delta t}+\mathbf{n}\times\frac{\mathrm{d}\mathbf{u}_b}{\mathrm{d}t}\right)\right]\mathrm{d}s+\mu\oint_{S_b}\mathbf{n}\times\boldsymbol{\omega}\,\mathrm{d}s \tag{30}$$

where ρ_f is the fluid density, μ is the dynamic viscosity, and $\mathbf{X}$ is the geometric centroid of the fish (though in Appendix A it is noted that the result holds for an arbitrary reference point, because of Kelvin's circulation theorem). The first integral represents the pressure contribution, and the second is the viscous contribution. It is noted that $\mathrm{d}\mathbf{u}_b/\mathrm{d}t$ is evaluated by a second-order central difference algorithm.

It is known that tail-beat frequency (in the form of Strouhal number defined with tail amplitude) is a key parameter in the propulsion mechanism of fish [4, 30]. Thus, in our work, we explored two different backbone frequencies at constant Reynolds number $Re_U=100$ based on free-stream U, which is set to unity. One frequency, $f=1$, produces net mean drag, whereas the other, $f=2.5$, produces net mean thrust.

DOI: 10.1002/fld

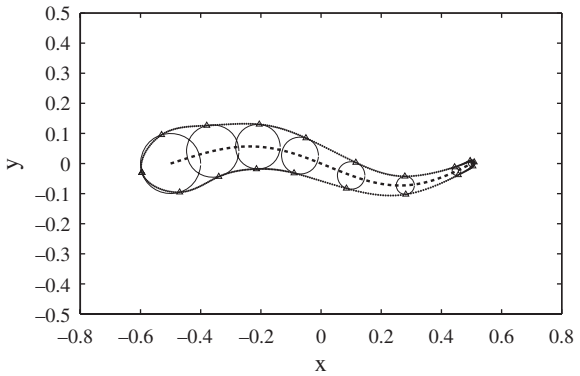

Figure 11. Schematic of the fish design: −− backbone, △ attachment points, and · skin panel centroids.

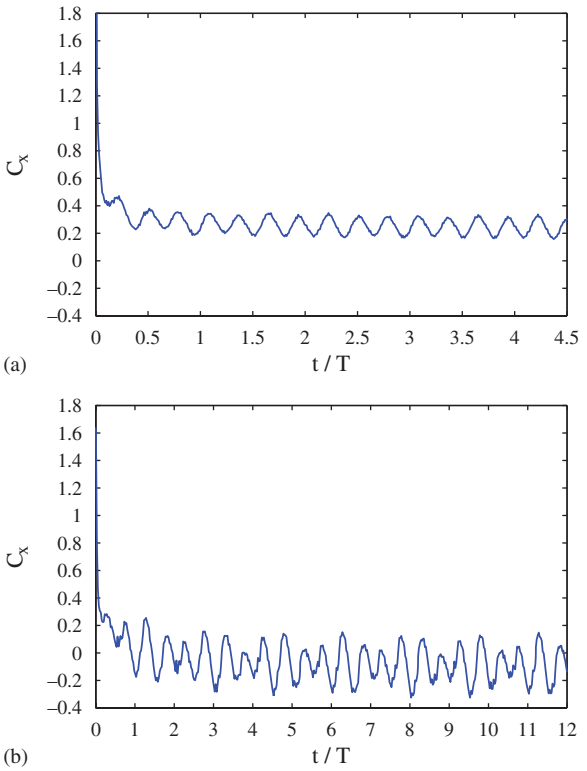

Figure 12. C_x *versus* time for undulating fish: (a) $f = 1$ and (b) $f = 2.5$.

DOI: 10.1002/fld

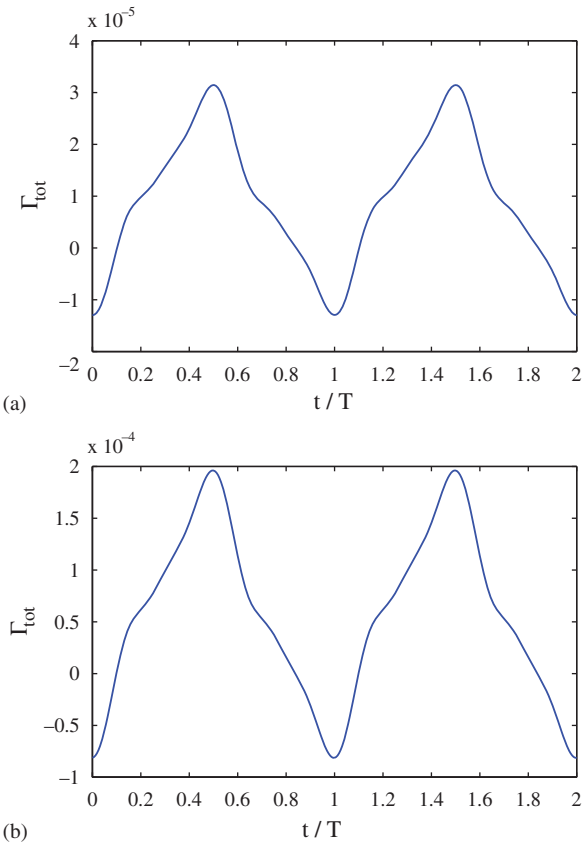

Figure 13. Total circulation *versus* time for undulating fish: (a) $f=1$ and (b) $f=2.5$.

In both cases, $\Delta x=0.005$ and $\Delta t=0.0025$. The resulting time histories of the x component of force are shown in Figure 12, in the form of the dimensionless coefficient $C_x=F_x/(\frac{1}{2}\rho U^2 L)$, where L is the horizontal length between the head and the tail (approximately 1.1 here). It is interesting to note that, for $f=1$, the dominant frequency is the natural shedding frequency of the static fish shape, which is quite close to the backbone oscillation frequency. However, in the $f=2.5$ case, the natural shedding frequency and forcing frequency are distinct, resulting in a more complicated history. The mean force coefficient, $\bar{C}_x$, in the case of $f=1$ is approximately 0.25 and in the case of $f=2.5$ is approximately -0.09. In each case, we also checked one numerical diagnostic, the total circulation variation with time, which should be zero because of enforcement of Kelvin's circulation theorem. Figure 13 plots the time-varying total circulation in both cases. The circulation remains very small and oscillatory.

Finally, Figures 14–15 present snapshots of vorticity contours corresponding to the two different frequencies. In the case of $f=1$, vorticity shedding and evolution from the fish tail demonstrate a classic Kármán vortex street. However, in the case of $f=2.5$, vorticity shedding and evolution show a reverse Kármán vortex street. In both cases, the low Reynolds number also contributes to thick boundary layers that are 'superimposed' on these wakes.

DOI: 10.1002/fld

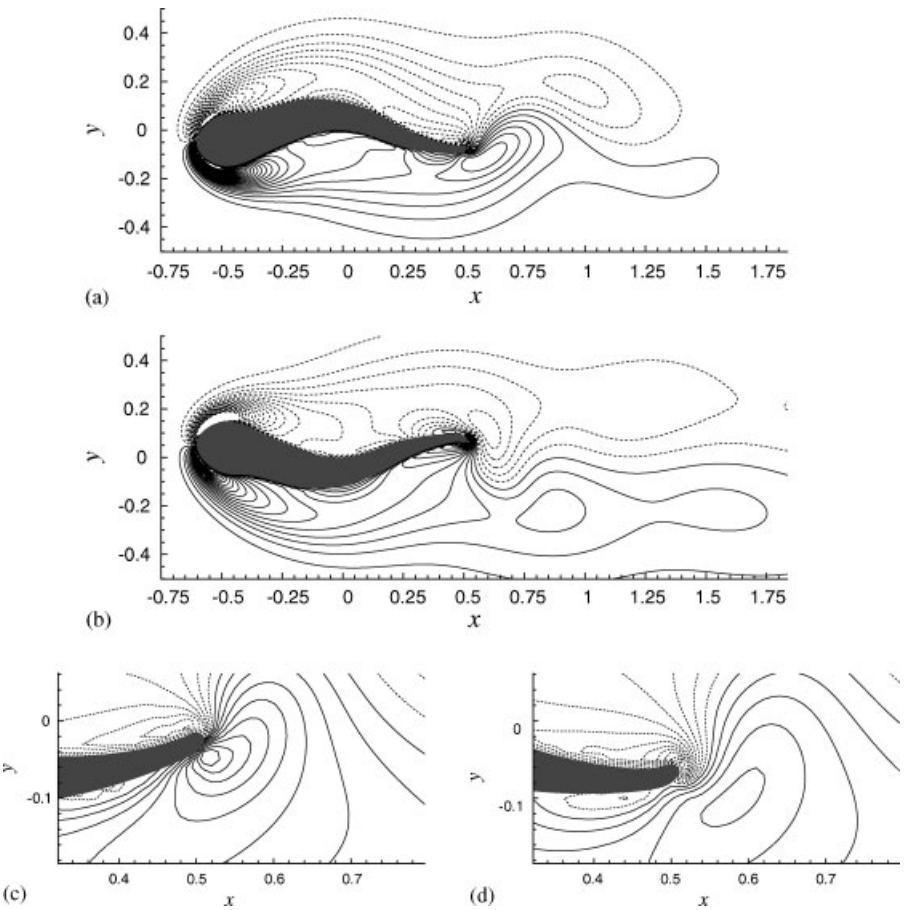

Figure 14. Full views and close-up views around fish tail of vorticity contours with $f=1$: (a) $t/T=1.18$; (b) $t/T=3.68$; (c) $t/T=2.05$; and (d) $t/T=2.15$.

4. CONCLUSIONS

With the goal to research the dynamics and mechanics of biolocomotion, we have developed, implemented and validated a VVPM for two-dimensional deforming bodies. In this paper, a technique to account for contribution from the prescribed surface motion to the velocities of the particles inside the flow has been derived. The validation has been carried out by comparison of simulation results with analytical solution for a periodically deforming circular cylinder immersed in a stagnant fluid. It has been shown that our velocity and vorticity profiles agree very well with the analytical solution and that the method converges at a reasonable rate. Finally, we explored the flow generated by kinematics of a simple undulatory fish-like motion. We investigated different backbone frequencies and demonstrated two standard situations, producing net mean drag and net mean thrust, respectively.

DOI: 10.1002/fld

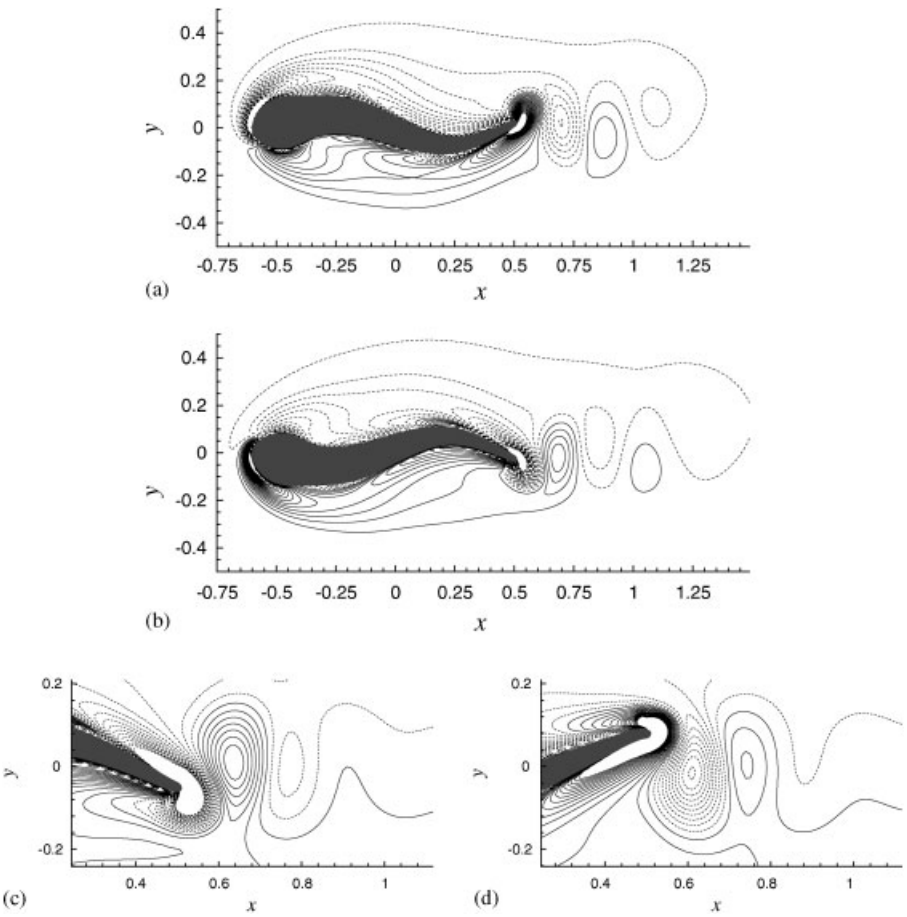

Figure 15. Full views and close-up views around fish tail of vorticity contours with $f=2.5$: (a) $t/T=1.96$; (b) $t/T=2.45$; (c) $t/T=11.39$; and (d) $t/T=11.78$.

In future work, this computational tool will be applied to explore several open questions of biological locomotion, including fish schooling behavior and free swimming two-dimensional fish-like shapes. The extension to three-dimensional simulations is ongoing.

APPENDIX A

Consider an arbitrary closed body immersed in a fluid, with constant area A_b and enclosed by surface contour S_b. It can be shown that the force exerted by the fluid on the body can be written in a fluid momentum-conservation form [31]

$$\mathbf{F}=-\rho_f\frac{\mathrm{d}\mathbf{P}}{\mathrm{d}t}+\frac{\mathrm{d}}{\mathrm{d}t}\int_{A_b}\rho_f\mathbf{u}_b\,\mathrm{d}A \tag{A1}$$

DOI: 10.1002/fld

where $\mathbf{P}$ is the linear impulse

$$\mathbf{P}=\int_{A_f}\mathbf{x}\times\boldsymbol{\omega}\,\mathrm{d}A+\int_{A_b}\mathbf{x}\times\boldsymbol{\omega}_b\,\mathrm{d}A \tag{A2}$$

and $\nabla\times\mathbf{u}_b=\boldsymbol{\omega}_b$. Note that $\mathbf{u}_b$ is only required to equal $\mathbf{u}$, the fluid velocity, on S_b, but is otherwise arbitrary. We also suppose that $\mathbf{u}_b$ is divergence-free, which is consistent with the assumption of constant area bounded by S_b. The time derivatives can be brought inside the integrals, resulting in

$$\mathbf{F}=-\rho_f\left[\int_{A_b}\mathbf{u}_b\times\boldsymbol{\omega}_b\,\mathrm{d}A+\int_{A_b}\mathbf{x}\times\frac{\mathrm{d}\boldsymbol{\omega}_b}{\mathrm{d}t}\,\mathrm{d}A-\int_{A_b}\frac{\mathrm{d}\mathbf{u}_b}{\mathrm{d}t}\,\mathrm{d}A+\int_{A_f}\mathbf{u}\times\boldsymbol{\omega}\,\mathrm{d}A+\int_{A_f}\mathbf{x}\times\frac{\mathrm{d}\boldsymbol{\omega}}{\mathrm{d}t}\,\mathrm{d}A\right] \tag{A3}$$

In addition, it can be shown that

$$\int_{A_b}\mathbf{u}_b\times\boldsymbol{\omega}_b\,\mathrm{d}A+\int_{A_f}\mathbf{u}\times\boldsymbol{\omega}\,\mathrm{d}A=0 \tag{A4}$$

Thus, Equation (A3) can be rewritten as

$$\mathbf{F}=-\rho_f\int_{A_b}\left(\mathbf{x}\times\frac{\mathrm{d}\boldsymbol{\omega}_b}{\mathrm{d}t}-\frac{\mathrm{d}\mathbf{u}_b}{\mathrm{d}t}\right)\mathrm{d}A-\rho_f\int_{A_f}\mathbf{x}\times\frac{\mathrm{d}\boldsymbol{\omega}}{\mathrm{d}t}\,\mathrm{d}A \tag{A5}$$

Note that, since $\int_{A_b}\boldsymbol{\omega}_b\,\mathrm{d}A+\int_{A_f}\boldsymbol{\omega}\,\mathrm{d}A=0$ by Kelvin's circulation theorem, $\mathbf{x}$ can be replaced with $\mathbf{x}-\mathbf{X}_c$, where $\mathbf{X}_c$ is arbitrary.

Now, we manipulate the integrand in the first integral in Equation (A5). In two dimensions,

$$\frac{\mathrm{d}\boldsymbol{\omega}_b}{\mathrm{d}t}=\nabla\times\frac{\mathrm{d}\mathbf{u}_b}{\mathrm{d}t} \tag{A6}$$

Then, we have

$$\mathbf{x}\times\left(\nabla\times\frac{\mathrm{d}\mathbf{u}_b}{\mathrm{d}t}\right)-\frac{\mathrm{d}\mathbf{u}_b}{\mathrm{d}t} \tag{A7}$$

However, $\mathbf{x}\times(\nabla\times\mathbf{a})-\mathbf{a}$ can be written as $\nabla(\mathbf{x}\cdot\mathbf{a})-\nabla\cdot(\mathbf{x}\mathbf{a})$ in two dimensions. Integrating over A_b and using the divergence theorem, we obtain

$$\int_{A_b}[\mathbf{x}\times(\nabla\times\mathbf{a})-\mathbf{a}]\,\mathrm{d}A=\int_{A_b}[\nabla(\mathbf{x}\cdot\mathbf{a})-\nabla\cdot(\mathbf{x}\mathbf{a})]\,\mathrm{d}A \tag{A8}$$

$$=\oint_{S_b}[\mathbf{n}(\mathbf{x}\cdot\mathbf{a})-(\mathbf{n}\cdot\mathbf{x})\mathbf{a}]\,\mathrm{d}s \tag{A9}$$

$$=\oint_{S_b}\mathbf{x}\times(\mathbf{n}\times\mathbf{a})\,\mathrm{d}s \tag{A10}$$

DOI: 10.1002/fld

where $\mathbf{n}$ is a unit normal directed into the fluid. Therefore, the force of fluid on the body, introducing $\mathbf{x}-\mathbf{X}_c$ for $\mathbf{x}$, becomes

$$\mathbf{F}=-\rho_f\int_{A_f}(\mathbf{x}-\mathbf{X}_c)\times\frac{\mathrm{d}\boldsymbol{\omega}}{\mathrm{d}t}\,\mathrm{d}A-\rho_f\oint_S(\mathbf{x}-\mathbf{X}_c)\times\left(\mathbf{n}\times\frac{\mathrm{d}\mathbf{u}_b}{\mathrm{d}t}\right)\mathrm{d}s \tag{A11}$$

It can be shown that, when the two-dimensional Navier–Stokes equations in vorticity transport form are introduced for $\mathrm{d}\boldsymbol{\omega}/\mathrm{d}t$, then the force can be written as

$$\mathbf{F}=-\rho_f\oint_{S_b}\left[(\mathbf{x}-\mathbf{X}_c)\times\left(-\nu\frac{\partial\boldsymbol{\omega}}{\partial n}+\mathbf{n}\times\frac{\mathrm{d}\mathbf{u}_b}{\mathrm{d}t}\right)+\nu\mathbf{n}\times\boldsymbol{\omega}\right]\mathrm{d}s \tag{A12}$$

When we introduce the Neumann condition on the vorticity flux, $\partial\boldsymbol{\omega}/\partial n=-\gamma/\Delta t$, we finally arrive at

$$\mathbf{F}=-\rho_f\oint_{S_b}\left[(\mathbf{x}-\mathbf{X}_c)\times\left(\frac{\gamma}{\Delta t}+\mathbf{n}\times\frac{\mathrm{d}\mathbf{u}_b}{\mathrm{d}t}\right)+\nu\mathbf{n}\times\boldsymbol{\omega}\right]\mathrm{d}s \tag{A13}$$

It is noted that the first part of this integral represents the contribution from surface pressure, whereas the second integral is the contribution from viscous stresses.

REFERENCES

1. Lighthill MJ. Note on the swimming of slender fish. *Journal of Fluid Mechanics* 1960; **9**(2):305–317.
2. Ellington CP. The aerodynamics of hovering insect flight. IV. Aerodynamic mechanisms. *Philosophical Transactions of the Royal Society of London, Series B* 1984; **305**(1122):79–113.
3. Triantafyllou MS, Triantafyllou GS, Yue DKP. Hydrodynamics of fishlike swimming. *Annual Review of Fluid Mechanics* 2000; **32**:33–53.
4. Anderson JM, Streitlien K, Barrett DS, Triantafyllou MS. Oscillating foils of high propulsive efficiency. *Journal of Fluid Mechanics* 1998; **360**:41–72.
5. Dickinson MH, Lehmann F-O, Sane SP. Wing rotation and the aerodynamic basis of insect flight. *Science* 1999; **284**(5422):1954–1960.
6. Chorin AJ. Numerical study of slightly viscous flow. *Journal of Fluid Mechanics* 1973; **57**:785–796.
7. Leonard A. Review: vortex methods for flow simulation. *Journal of Computational Physics* 1980; **37**(3):289–335.
8. Cottet G-H, Koumoutsakos P. *Vortex Methods*: *Theory and Practice*. Cambridge University Press: Cambridge, 2000.
9. Koumoutsakos P. Multiscale flow simulations using particles. *Annual Review of Fluid Mechanics* 2005; **37**: 457–487.
10. Greengard L, Rokhlin V. A fast algorithm for particle simulations. *Journal of Computational Physics* 1987; **73**(2):325–348.
11. Carrier J, Greengard L, Rokhlin V. A fast adaptive multipole algorithm for particle simulations. *SIAM Journal on Scientific and Statistical Computing* 1988; **9**(4):669–686.
12. Degond P, Mas-Gallic S. The weighted particle method for convection–diffusion equations. Part 1: The case of an isotropic viscosity. *Mathematics of Computation* 1989; **53**(188):485–507.
13. Eldredge JD, Leonard A, Colonius T. A general deterministic treatment of derivatives in particle methods. *Journal of Computational Physics* 2002; **180**(2):686–709.
14. Koumoutsakos P, Leonard A, Pépin F. Boundary conditions for viscous vortex methods. *Journal of Computational Physics* 1994; **113**(1):52–61.
15. Koumoutsakos P, Leonard A. High-resolution simulations of the flow around an impulsively started cylinder using vortex methods. *Journal of Fluid Mechanics* 1995; **296**:1–38.
16. Ploumhans P, Winckelmans GS. Vortex methods for high-resolution simulations of viscous flow past bluff bodies of general geometry. *Journal of Computational Physics* 2000; **165**(2):354–406.

DOI: 10.1002/fld

17. Ploumhans P, Winckelmans GS, Salmon JK, Leonard A, Warren MS. Vortex methods for direct numerical simulation of three-dimensional bluff body flows: application to the sphere at $Re = 300$, 500, and 1000. *Journal of Computational Physics* 2002; **178**(2):427–463.
18. Cottet G-H, Poncet P. Advances in direct numerical simulations of 3D wall-bounded flows by Vortex-in-Cell methods. *Journal of Computational Physics* 2004; **193**(1):136–158.
19. Eldredge JD. Numerical simulation of the fluid dynamics of 2D rigid body motion with the vortex particle method. *Journal of Computational Physics* 2007; **221**(2):626–648.
20. Peskin CS. The fluid dynamics of heart valves: experimental, theoretical and computational methods. *Annual Review of Fluid Mechanics* 1981; **14**:235–259.
21. Zhu L, Peskin C. Interaction of two flapping filaments in a flowing soap film. *Physics of Fluids* 2003; **15**(7): 1954–1960.
22. Mittal R, Iaccarino G. Immersed boundary methods. *Annual Review of Fluid Mechanics* 2005; **37**:239–261.
23. Ramamurti R, Sandberg WC. A three-dimensional computational study of the aerodynamic mechanisms of insect flight. *Journal of Experimental Biology* 2002; **205**:1507–1518.
24. Ramamurti R, Sandberg WC, Löhner R, Walker JA, Westneat MW. Fluid dynamics of flapping aquatic flight in the bird wrasse: three-dimensional unsteady computations with fin deformation. *Journal of Experimental Biology* 2002; **205**:2997–3008.
25. Cottet G-H. A particle model for fluid-structure interaction. *Comptes Rendus de l' Academie des Sciences de Paris*, *Serie I* 2002; **335**:833–838.
26. Cottet G-H, Poncet P. Advances in direct numerical simulations of 3D wall-bounded flows by vortex-in-cell methods. *Journal of Computational Physics* 2003; **193**:136–158.
27. Leonard A, Shiels D, Salmon JK, Winckelmans GS, Ploumhans P. Recent advances in high resolution vortex methods for incompressible flows. *Thirteenth AIAA Computational Fluid Dynamics Conference*, Snowmass Village, CO, 1997.
28. Cottet G-H, Koumoutsakos P, Salihi MLO. Vortex methods with spatially varying cores. *Journal of Computational Physics* 2000; **162**(1):164–185.
29. Lighthill MJ. Aquatic animal propulsion of high hydromechanical efficiency. *Journal of Fluid Mechanics* 1970; **44**(2):265–301.
30. Fish FE, Lauder GV. Passive and active flow control by swimming fishes and mammals. *Annual Review of Fluid Mechanics* 2006; **38**:193–224.
31. Wu JC. Theory of aerodynamic force and moment in viscous flows. *AIAA Journal* 1981; **195**(4):432–441.

DOI: 10.1002/fld